Scripta Materialia 202 (2021) 113985

Contents lists available at ScienceDirect

Scripta Materialia

journal homepage: www.elsevier.com/locate/scriptamat

Role of deformation twinning in fatigue of CrCoNi medium-entropy alloy at room temperature

Milan Heczko[a,b,c,**,*], Veronika Mazánová[a,b,c,**], Connor E. Slone[d], Mulaine Shih[b], Easo P. George[e,f], Maryam Ghazisaeidi[b], Jaroslav Polák[c], Michael J. Mills[a,b]

[a] Center for Electron Microscopy and Analysis, The Ohio State University, Columbus, OH, 43212, USA
[b] Department of Materials Science and Engineering, The Ohio State University, Columbus, OH 43210, USA
[c] Institute of Physics of Materials, Czech Academy of Sciences, Žižkova 22, 616 00 Brno, Czech Republic
[d] Materials and Corrosion Engineering Practice, Exponent, Inc., 149 Commonwealth Drive, Menlo Park, CA 94025, USA
[e] Materials Science and Technology Division, Oak Ridge National Laboratory, Oak Ridge, TN 37831, USA
[f] Materials Science and Engineering Department, University of Tennessee, Knoxville, TN 37996, USA

ARTICLE INFO

Article history:
Received 7 April 2021
Revised 3 May 2021
Accepted 3 May 2021
Available online 24 May 2021

Keywords:
Medium- and high-entropy Alloys
Deformation twinning
Fatigue
Crack initiation
Persistent slip marking

ABSTRACT

Cylindrical specimens of CrCoNi alloy with electropolished surfaces were subjected to constant total strain amplitude low cycle fatigue. The alloy exhibited an initial period of cyclic hardening followed by cyclic softening until failure occurred. At the end of hardening stage at the peak of cyclic stress, well-developed persistent slip markings (PSMs) consisting of extrusions and intrusions were associated with thin deformation twins. A sophisticated experimental workflow was designed to extract information from the surface and the bulk of tested material. A combination of SEM, EBSD, ECCI, FIB and HR-STEM was used to study the internal structure and the surface profiles around the deformation twins, which were produced during the initial period of cyclic loading. Furthermore, localized cyclic plastic strain and stress concentrations near deformation twins led not only to early, well-developed PSMs, but also to the activation of TWIP and TRIP plasticity even at low macroscopic stress amplitudes.

1. Article

Medium- and high-entropy alloys (MEAs/HEAs) have been recognized for their outstanding ductility, fracture toughness, and high work hardening rates under monotonic loading conditions [1–3]. Although many alloy compositions have been examined, model systems such as equiatomic CrMnFeCoNi (the Cantor alloy), and its subset, equiatomic CrCoNi, have received particular attention and have been extensively studied, especially in monotonic tensile and compressive loading [4–6]. Both are single phase, solid solution alloys with face-centered cubic (FCC) structures and low stacking fault energies (SFE) that promote planar slip and deformation twinning (DTW). The equiatomic CrCoNi alloy has superior properties to the parent CrMnFeCoNi alloy, including higher yield strength, elongation, fracture toughness, and work hardening rate [5,7].

Fatigue studies of MEAs/HEAs are relatively recent and have focused on general alloy performance and microstructures at the end of fatigue life [8,9]. An initial hardening stage followed by cyclic softening has been commonly observed, consistent with behavior in TWIP steels [10]. In low cycle fatigue (LCF) studies, post-mortem analyses of CrMnFeCoNi have shown planar slip and dislocation pile-ups at grain boundaries (including annealing twin boundaries (ATB) formed prior to testing). Reports of DTW have been inconsistent [10,11]. Lu et al. [9], in the only study that used cylindrical test specimens rather than flat, rectangular specimens, examined both CrMnFeCoNi and CrCoNi and did not report DTW in either alloy. Disagreement over the presence of DTW has also been reported for high-cycle fatigue studies of CrMnFeCoNi [12,13]. Little work has been performed to understand the early stages of cyclic strain localization in these alloys. Given discrepancies in the literature regarding DTW and the absence of detailed studies regarding behavior at early cycles, this work focuses on cyclic strain localization, development of surface relief and fatigue crack initiation, and the role of DTW therein.

Equiatomic CrCoNi alloy was produced by arc melting following vacuum homogenization at 1200 °C for 24 h [14]. The material was rolled and annealed at 900 °C for 1 h to obtain the final recrystal-

* Corresponding author.
E-mail addresses: heczko.2@osu.edu, heczko@ipm.cz (M. Heczko).
** Present address: The Ohio State University, Department of Materials Science and Engineering, Center for Electron Microscopy and Analysis (CEMAS), 1305 Kinnear Rd, Suite 100, Columbus, OH 43212, USA.

https://doi.org/10.1016/j.scriptamat.2021.113985
1359-6462/

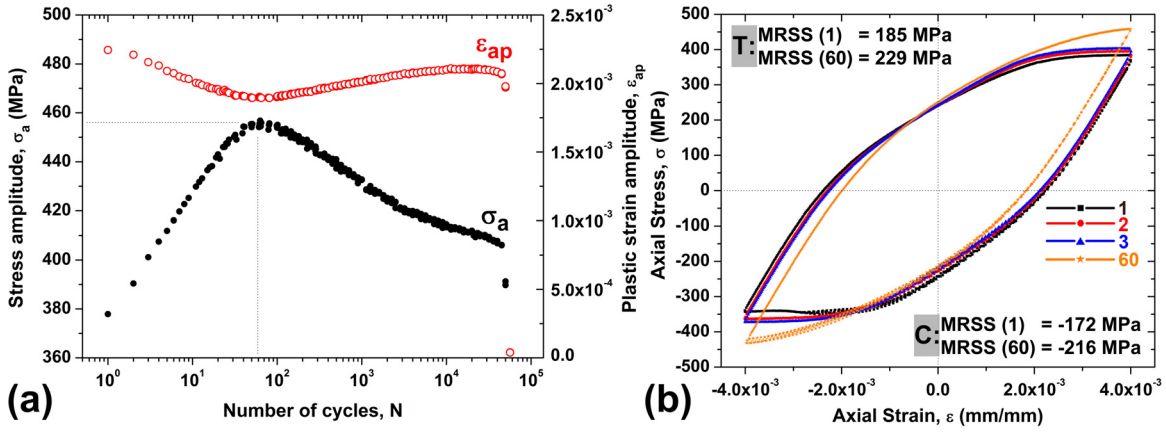

Fig. 1. (a) Cyclic hardening/softening curve of CrCoNi loaded with total strain amplitude of 0.4%. Stress amplitude σ_a and corresponding plastic strain amplitude ε_{ap} are plotted versus number of cycles N. Peak of cyclic stress amplitude is marked by gray lines extending to the plot axes. (b) Comparison of selected hysteresis loops and corresponding calculated MRSS for tensile (T) and compressive (C) part of selected loops.

lized microstructure with an average grain size of 21 μm (see **Fig. S1** and further details regarding the grain size measurement in the **Supplementary Material**).

Cylindrical fatigue specimens were machined from the recrystallized sheets/plates by electrical discharge machining (EDM) with their longitudinal axes parallel to the rolling direction of the sheet. The specimens had a diameter of 2.3 mm and a gauge length of 9 mm [15,16]. After fabrication by EDM, the gauge section of the specimens was mechanically and electrolytically polished [14]. Fatigue tests were performed using a computer controlled electro-hydraulic MTS 810 system with Flextest software. Mechanical grips held at constant temperature were used and strain was measured and controlled with an 8 mm base axial extensometer. Specimens were cyclically strained in a fully reversed symmetrical cycle (R_ε = -1) with total strain control and constant total strain rate of 2×10^{-3} s^{-1}.

To preserve features on sample surfaces after mechanical testing, whole specimens were put into the large chamber of a dual-beam scanning electron microscope (SEM) with a focused ion beam (FIB). SEMs TESCAN Lyra3 XMU and Thermo Fisher Scientific (TFS) Apreo equipped with electron back-scatter diffraction (EBSD) detectors from EDAX were used with OIM TSL software. A combination of SEM, EBSD, electron channeling contrast imaging (ECCI) and FIB was used for characterization of fatigue-induced surface relief. The profiles of persistent slip markings (PSM) developed on the surface were observed and documented simultaneously with the underlying microstructure using site- and orientation-specific TEM surface lamella preparation by FIB [17–19]. Thin foils were studied using an image-corrected and mono-chromated TFS/FEI Titan-Themis 60-300 kV scanning transmission electron microscope (STEM) [20].

Equiatomic CrCoNi was subjected to strain-controlled LCF tests at room temperature in a wide interval of strain amplitudes ranging from 0.3 to 0.8%. Although multiple strain amplitudes were tested, only data for total strain amplitude of 0.4% are presented in the current work. In **Fig. 1a**, the evolution of the stress amplitude σ_a and the corresponding plastic strain amplitude ε_{ap} with the number of cycles N is shown. The cyclic response of CrCoNi is characterized by an initial cyclic hardening stage for 60 cycles, followed by a cyclic softening stage (99.8% of N_f) until fracture (N_f = 50729). The focus of the current work is on samples interrupted at the peak of cyclic stress amplitude, i.e. after 60 loading cycles at 0.4% total strain amplitude (corresponding to 0.21% plastic strain amplitude at the 60th cycle).

Selected hysteresis loops are plotted in **Fig. 1b**. During the initial cyclic hardening stage, the stress amplitude increased from 378 MPa in the 1st cycle to 456 MPa in the 60th cycle. At the peak of cyclic stress amplitude in the 60th cycle, the maximum resolved shear stresses (MRSS, Schmid factor m = 0.5) were 229 MPa and 216 MPa for tensile and compressive parts of the loop, respectively.

The fatigue-induced surface relief was studied using a combination of high-resolution SEM (secondary electron imaging mode, SE, and backscattered electron imaging mode, BSE), ECCI, and EBSD. **Fig. 2** shows typical surface features and the microstructure of CrCoNi at the end of hardening (60 cycles at 0.4% strain amplitude). While SE imaging mode is sensitive to surface information and reveals distinctive PSMs developed on the surface (**Fig. 2a**), BSE/ECCI imaging documents underlying microstructure characteristics like individual dislocations, extended stacking faults (SF), and most importantly, narrow linear features consistent with deformation twins. The most striking observation is that deformation twins are found exactly at locations where developed PSMs emerge on the surface (**Fig. 2b**).

Notably, not every grain had distinct PSMs developed on the surface in this early stage of fatigue life. However, as shown later, our results prove that every distinctly developed PSM studied after 60 cycles was associated with thin (≈30 nm) deformation twins. Therefore, attention was focused on characterizing grains with distinctly developed PSMs. EBSD maps paired with SE/BSE images were used to correlate PSM formation with the crystallographic orientation of each grain. A typical EBSD map showing crystallographic orientations parallel to the loading axis is shown in **Fig. 2c**. Detail in **Fig. 2d** demonstrates one of the analyzed grains with developed PSMs using SE imaging. **Fig. 2e** shows the basic stereographic triangle marking orientations of grains with distinctly developed PSMs and deformation twins.

To reveal the real profile of developed PSMs and the corresponding fatigue-induced microstructure, FIB sectioning and site- and orientation-specific S/TEM thin foils were extracted [17–19]. **Fig. 3a** shows several early, well developed PSMs oriented at 76 degrees with respect to the loading axis, suggesting these PSMs are associated with high Schmid factor slip planes. FIB sectioning perpendicular to the PSM profiles, denoted by the red dashed line in **Fig. 3a**, reveals that early developed PSMs were indeed associated with deformation twins. Contrast reversal in the SEM-SE image in **Fig. 3b** is characteristic of twinning.

PSMs are formed by paired intrusions and extrusions on the surface of the material [18,21–25]. Detail of PSM B in **Fig. 3c** shows a shallow intrusion on the left interface of the deformation twin, and an extrusion on the right interface. The thickness of the deformation twin was approximately 38 nm based on the thickness of the orientation contrast reversal band. The size of the correspond-

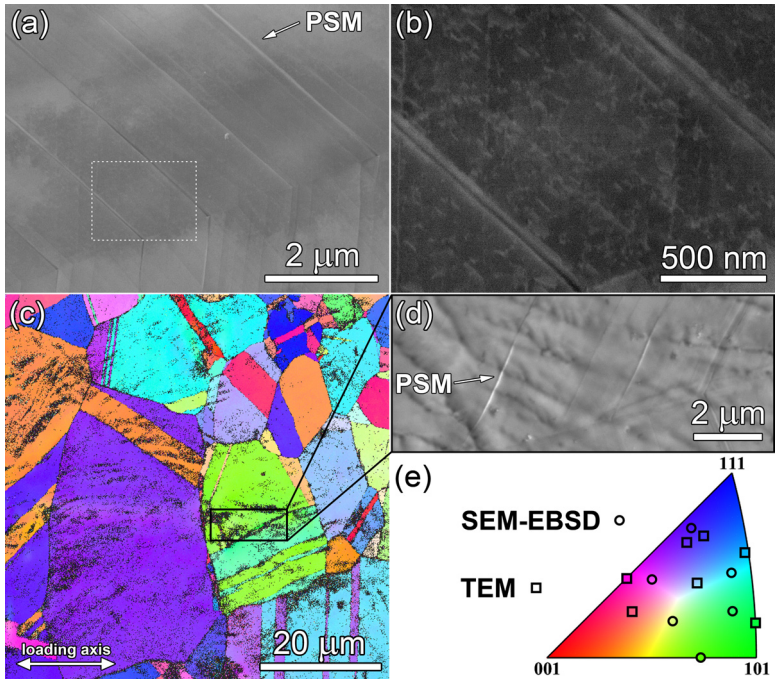

Fig. 2. CrCoNi microstructure after 60 cycles at 0.4% strain amplitude. (a) SEM-SE image showing examples of early developed PSMs on the surface. (b) SEM-BSE image showing dislocations and narrow linear features consistent with deformation twins at the locations where PSMs emerge on the surface. Detail is from the location marked by white dashed rectangle in (a). (c) Typical EBSD map showing crystallographic orientations parallel to the loading axis. Points with confidence index lower than 0.02 were removed. (d) Detail of one of the analyzed grains with developed PSMs revealed by SEM-SE. (e) Orientations of grains with distinctive developed PSMs. Orientations determined from SEM-EBSD (circles) are complemented with grain orientations where deformation twinning was confirmed by HR-STEM (rectangles).

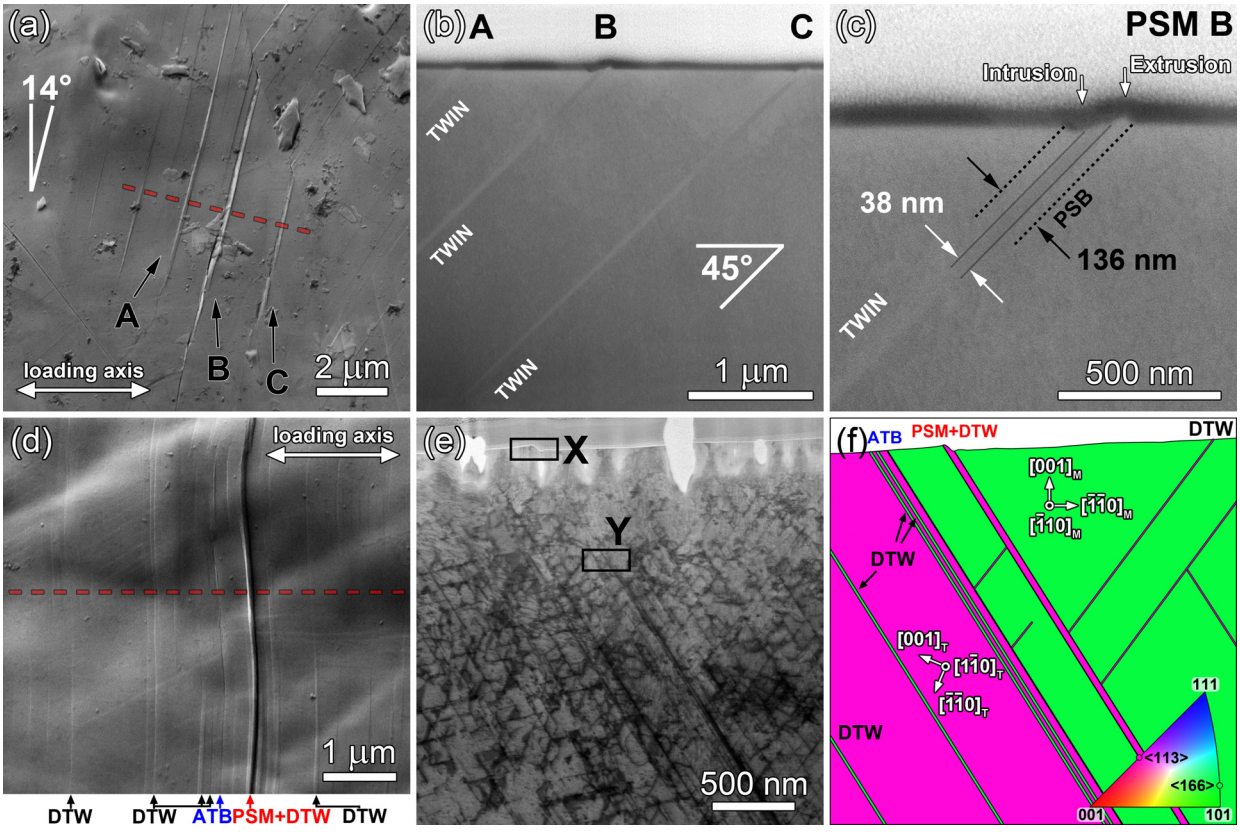

Fig. 3. (a) SEM-SE image showing well-developed PSMs on the surface with red line indicating the location of FIB sectioning. (b) SEM-BSE image of the FIB cut shows that the PSM profiles from (a) are associated with deformation twins. (c) Detail reveals that PSM B consists of extrusion and intrusion. (d) A second example of a well-developed PSM on the surface. (e) BF-STEM DCI image of FIB foil extracted from the location marked with red dashed line in (d). (f) Loading axis orientation based colored map corresponding to the area from (e) marks the positions of ATB, deformation twins and nano-twins. Images (e, f) were taken with the electron beam parallel to $[\bar{1}10]_M$ and $[1\bar{1}0]_T$ directions.

ing persistent slip band (PSB) was approximately 136 nm based on the distance between the intrusion and extrusion.

Fig. 3d shows a different grain with an early developed PSM where the TEM lamella was extracted (red dashed line) using FIB. The underlying deformation structure was studied in detail by STEM and is shown in **Fig. 3e** using bright field (BF)-STEM diffraction contrast imaging (DCI). Grain orientations with respect to the loading axis and the positions of deformation twins, nano-twins and ATB are marked in the schematic map in **Fig. 3f**. Orientations displayed on the map were manually determined from STEM/CBED diffraction patterns and no full-field mapping techniques were used. The early developed PSM was associated with a deformation twin of thickness 31 nm (equal to 150 {111} planes for a lattice parameter of 0.3567 nm [7]). Interestingly, at this stage of fatigue life, no PSM profile was associated with the ATB, nor with any of the other thin nano-twins, which had thicknesses varying from 1 to 10 nm.

A high-angle annular dark field (HAADF)-STEM image of the PSM profile (the area marked by letter "X" in **Fig. 3e**) is depicted in **Fig. 4a**. The profile is observed along $[\bar{1}10]_M/[1\bar{1}0]_T$ zone axes with the primary slip and twinning planes $(11\bar{1})_{M/T}$ oriented edge-on. Positions of two twin/matrix interfaces highlighted by white dashed lines were determined using atomic resolution STEM. The red dashed line marks a 22 nm step which would be induced on a perfectly flat surface by formation of a 31 nm thick deformation twin (step size calculation is described in **Supplementary Material**). Notably, in this $[66\bar{1}]$ oriented grain with DTW+PSM, twinning is more favorable since it has Schmid factor $m\{[112](11\bar{1})\} = 0.420$, which is higher than perfect dislocation glide with $m\{[011]/[101](11\bar{1})\} = 0.364$.

In **Fig. 4b**, the PSM profile is visualized by plotting its height measured in the direction of the trace of primary slip plane (i.e., along the [112] direction) relative to the undisturbed surface of the grain versus the distance in the direction of PSB width, i.e. along the $[11\bar{1}]$ direction [17]. The PSM consists of an extrusion and intrusion on the left and right sides of a coherent $\Sigma 3$ twin interface, respectively. After 60 loading cycles with total strain amplitude 0.4%, the extrusion height was 36 nm and the intrusion depth was 12 nm. If the calculated twin-induced step of 22 nm is subtracted, the extrusion height is 14 nm, which is still slightly larger than the intrusion depth. Based on extensive work on other alloys, development of a smooth PSM profile with an extrusion/intrusion of these dimensions requires at least several tens of loading cycles [26,27]. This suggests the deformation twin was formed early during cyclic loading, prior to the further development of the extrusion/intrusion profile. This is also consistent with the initial state of the alloy where no thin annealing twins (i.e. < 300 nm thickness) were found even using HR-STEM.

Notably, we observed PSMs at deformation twins in this early stage of cyclic loading, but not other sites such as ATBs. It is well known that in FCC alloys, ATBs play a significant role in the localization of cyclic plastic deformation and subsequent fatigue crack nucleation [28,29]. In general, this has been rationalized based on elastic incompatibility between the annealing twin and the parent grain. Additional internal stresses are generated near ATBs to maintain strain compatibility at the boundaries, which act in concert with resolved shear stresses from the applied loads to cause PSB formation and, eventually, crack initiation [24,30–33]. Dislocations may also pile up at ATBs, leading to strain localization and crack initiation [34,35].

Following the extended model by Heinz and Neumann [30] and Blochwitz and Tirschler [33], the additional shear stress τ_{SF}, developed at the twin boundaries in CrCoNi was calculated using the elastic constants from Laplanche et al. [36]. The estimated additional τ_{SF} ranges from -33 to 112 MPa for external applied stress $\sigma = 370$ MPa under tension in the first loading cycle, depending on the value of relative plastic strain as shown in **Fig. S3b**. For the sake of brevity, further details are described in **Supplementary Material**. Our results show that thin, ideally oriented deformation twins may be even more potent stress concentrators than ATBs, and therefore more important to early PSB development and crack initiation. Further modeling efforts are currently in progress to assess the effect of twin width on stress field superposition.

Evidence of extreme stress concentration and cyclic strain localization is visible around the 31 nm deformation twin shown in **Fig. 4**. Near the left twin/matrix interface (**Fig. 4c**), approx. 10 nm into the deformation twin, a stack of about twelve {111} planes of intensive slip is observed. This band comprises a mixture of defects, including SFs of dissociated 1/2<110> dislocations [37,38], extrinsic stacking faults (ESF), nano-twins (TWIN), and even truncated short "lens-shaped" hexagonal-close packed (HCP) regions. FFT filtered HAADF-STEM images of the defect types are shown in **Figs. 4d-g** accompanied by the center of symmetry maps, further highlighting the differences in the stacking sequence [38]. The cumulative cyclic plastic strain localized near deformation twins can lead to TWIP and TRIP effects even in cyclic loading with low strain amplitudes.

Although a full discussion of crack initiation is beyond the scope of this work and will be addressed in a follow-on study, deformation twins evidently play a pivotal role in early cyclic plastic strain localization and PSB development in CrCoNi. Continuous production and annihilation of edge dislocations on the neighbor planes, and non-conservative jog motion on screw dislocations, results in the steady formation of point defects. Provided at least one type of point defect is mobile at room temperature, its migration and later annihilation facilitates mass redistribution over short distances and a rudimentary PSM consisting of extrusion and an intrusion is produced [26,27]. Extrusions and intrusions grow during cyclic straining, and at the tip of a crack-like intrusion, a stage I fatigue crack is produced. Deformation twins that develope at the onset of cyclic plastic straining thus add not only to the hardening of the material, providing strong barriers to secondary slip systems as in monotonic deformation [39], but also contribute to more intensive damage evolution by facilitating fatigue crack initiation.

The formation of the first deformation twins during cyclic loading are likely facilitated by stress concentrations arising from ATBs and/or high angle grain boundaries (HAGBs). In monotonic tensile loading, the onset of twinning in CrCoNi was not observed at room temperature until specimens reached true strains greater than 9.7%, corresponding to a true stress of 790 ± 100 MPa (equivalent to a resolved shear stress of 260 ± 30 MPa) [6]. These are much larger strains and stresses than were observed in this work: at the peak of stress amplitude, the maximum tensile stress was 458 MPa, corresponding to a resolved shear stress of 229 MPa for even the most ideally oriented grain (Schmid factor $m = 0.5$). Deformation twins such as the one shown in **Fig. 4** were well-developed by the peak of stress amplitude and must have initiated early during testing. Once deformation twins initiated near ATBs and/or HAGBs, thin deformation twins became sites of even greater stress concentration and facilitated development of PSBs.

While the cyclic hardening stage is characterized by increasing dislocation and twin density and their mutual interactions, further cyclic loading causes softening for most of the fatigue life. Although the details are beyond the scope of the present work, which focuses on the role of deformation twinning during the hardening stage, the cyclic softening response can be qualitatively attributed to two mechanisms. First, at all strain amplitudes, PSBs become well-established after the initial hardening period and subsequently act as easy glide paths. Cyclic plastic deformation is localized preferentially in these bands. In CrCoNi, PSBs consist either of irregular arrangements of ordinary dislocations (i.e., alternating dislocation rich and poor areas, similar to PSBs reported in

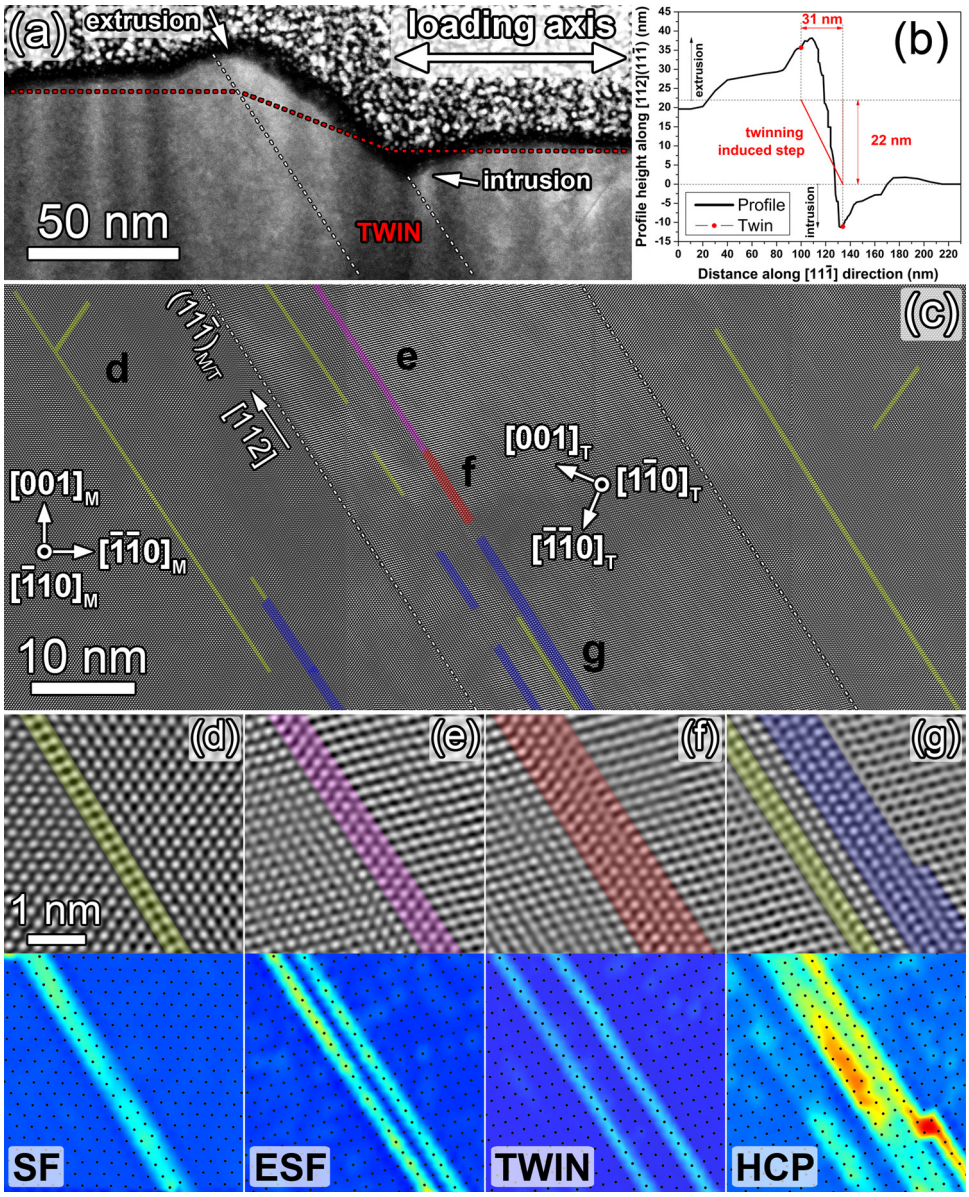

Fig. 4. (a) Detail of the area X from Fig. 3**e** shows PSM consisting of extrusion and intrusion associated with the deformation twin. Red dotted line marks twinning induced step calculated from the twin thickness. Positions of the twin/matrix interface highlighted by white dashed lines were determined by HR-STEM. (b) Measured height of the PSM in the direction of the trace of the primary slip plane versus the distance measured in the direction of the width of PSB. (c) FFT filtered HR-STEM atomic resolution map of area Y from Fig. 3**e** indicating locations of defects such as SF (d), ESF (e), nano-TWIN (f) and HCP bands (g). FFT filtered images on top are complemented by center of symmetry maps on bottom. All images were taken with the electron beam parallel to $[\bar{1}10]_M$ and $[1\bar{1}0]_T$ directions.

other FCC alloys with low SFE, e.g. [17,40]), or of a mixture of defect types as shown in Fig. 4**c**. The second cyclic softening mechanism is the rearrangement of planar dislocation structures into configurations with lower stored internal strain energy [41–43], such as veins, wall/channel structures, or even dislocation cells, as was confirmed recently in CrCoNi and CrMnFeCoNi [9]. The mechanism becomes more prevalent for larger strain amplitudes, which activate several slip systems in properly oriented grains. Rearrangement of the dislocation structures occurs through mutual interactions such as annihilation or multi-pole formation [41,42]. Interestingly, at the end of the fatigue life, CrCoNi alloy still retains about 35% of the increase of the cyclic strength reached during the initial hardening stage (Fig. 1**a**). This behavior is in contrast with other FCC alloys with low SFE (e.g. Fe-25Ni-22.5Cr alloy Sanicro 25 [40]) whose cyclic strength at the end of the softening stage is much lower than in the initial state.

In summary, the LCF response of equiatomic CrCoNi alloy at 0.4% constant strain amplitude comprised an initial period of cyclic hardening for 60 cycles, followed by cyclic softening until failure. Analysis of a sample interrupted at the end of the hardening stage, i.e. at the peak of cyclic stress showed that PSMs consisting of extrusions and intrusions were already present at this early stage of testing, and every observed PSM was associated with deformation twin. Localized cyclic plastic strain and stress concentrations led to activation of TWIP and TRIP plasticity even at low macroscopic stress amplitudes.

Notice of copyright

Declaration of Competing Interest

The authors declare that they have no known competing financial interests or personal relationships that could have appeared to influence the work reported in this paper.

Acknowledgements

MH, VM, MS, MG, and MJM acknowledge financial support from the National Science Foundation under the contract No. #DMR-1905748. EPG is supported by the U.S. Department of Energy, Office of Science, Basic Energy Sciences, Materials Sciences and Engineering Division. MH acknowledges support from the Thermo Fisher Scientific & Czechoslovak Microscopy Society fellowship. Authors would like to thank Jiří Tobiáš and Dr. Ivo Kuběna for their help with the mechanical testing of material and Dagmar Herzánová and Prof. Dr. Tomáš Kruml for the preparation of twin-jet electropolished disc foils.

Supplementary materials

Supplementary material associated with this article can be found, in the online version, at doi:10.1016/j.scriptamat.2021.113985.

References

[1] Z. Li, S. Zhao, R.O. Ritchie, M.A. Meyers, Prog. Mater Sci. 102 (2019) 296–345.
[2] B. Gludovatz, A. Hohenwarter, D. Catoor, E.H. Chang, E.P. George, R.O. Ritchie, Science 345 (2014) 1153–1158.
[3] D.B. Miracle, O.N. Senkov, Acta Mater. 122 (2017) 448–511.
[4] F. Otto, A. Dlouhý, Ch. Somsen, H. Bei, G. Eggeler, E.P. George, Acta Mater. 61 (2013) 5743–5755.
[5] B. Gludovatz, A. Hohenwarter, K.V.S. Thurston, H. Bei, Z. Wu, E.P. George, R.O. Ritchie, Nat. Commun. 7 (2016) 10602.
[6] J. Miao, C.E. Slone, T.M. Smith, C. Niu, H. Bei, M. Ghazisaeidi, G.M. Pharr, M.J. Mills, Acta Mater. 132 (2017) 35–48.
[7] G. Laplanche, A. Kostka, C. Reinhart, J. Hunfeld, G. Eggeler, E.P. George, Acta Mater. 128 (2017) 292–303.
[8] S.M. Vakili, A. Zarei-Hanzaki, A.S. Anoushe, H.R. Abedi, M.H. Mohammad-Ebrahimi, M. Jaskari, S.S. Sohn, D. Ponge, L.P. Karjalainen, Acta Mater. 185 (2020) 474–492.
[9] K. Lu, A. Chauhan, M. Walter, A.S. Tirunilai, M. Schneider, G. Laplanche, J. Freudenberger, A. Kauffmann, M. Heilmaier, J. Aktaa, Scr. Mater. 194 (2021) 113667.
[10] S.A.A. Shams, G. Jang, J.W. Won, J.W. Bae, H. Jin, H.S. Kim, C.S. Lee, Mater. Sci. Eng. 792 (2020) 139661.
[11] A.G. Wang, X.H. An, J. Gu, X.G. Wang, L.L. Li, W.L. Li, M. Song, Q.Q. Duan, Z.F. Zhang, X.Z. Liao, J. Mater. Sci. Technol. 39 (2020) 1–6.
[12] Y.Z. Tian, S.J. Sun, H.R. Lin, Z.F. Zhang, J. Mater. Sci. Technol. 35 (2019) 334–340.
[13] Y.-K. Kim, G.-S. Ham, H.S. Kim, K.-A. Lee, Intermetallics 111 (2019) 106486.
[14] C.E. Slone, J. Miao, E.P. George, M.J. Mills, Acta Mater. 165 (2019) 496–507.
[15] T. Hirose, H. Sakasegawa, A. Kohyama, Y. Katoh, H. Tanigawa, J. Nucl. Mater. 283–287 (2000) 1018–1022.
[16] I. Kuběna, T. Kruml, P. Spätig, N. Baluc, Z. Oksiuta, M. Petrenec, K. Obrtlík, J. Polák, Proc. Eng. 2 (2010) 717–724.
[17] J. Polák, V. Mazánová, M. Heczko, I. Kuběna, J. Man, Fatigue Fract. Eng. Mater. Struct. 40 (2017) 1101–1116.
[18] J. Polák, V. Mazánová, M. Heczko, R. Petráš, I. Kuběna, L. Casalena, J. Man, Eng. Fract. Mech. 185 (2017) 46–60.
[19] V. Mazánová, M. Heczko, C. Slone, I. Kuběna, J. Tobiáš, E. George, T. Kruml, J. Polák, M. Mills, Microsc. Microanal. 26 (2020) 2224–2225.
[20] P.J. Phillips, M.C. Brandes, M.J. Mills, M. De Graef, Ultramicroscopy 111 (2011) 1483–1487.
[21] Z.S. Basinski, S.J. Basinski, Scripta Metall. 18 (1984) 851–856.
[22] Z.S. Basinski, S.J. Basinski, Acta Metall. 37 (1989) 3263–3273.
[23] Z.S. Basinski, S.J. Basinski, Prog. Mater Sci. 36 (1992) 89–148.
[24] A. Hunsche, P. Neumann, Acta Metall. 34 (1986) 207–217.
[25] J. Man, P. Klapetek, O. Man, A. Weidner, K. Obrtlík, J. Polák, Philos. Mag. 89 (2009) 1337–1372.
[26] J. Polák, J. Man, Mater. Sci. Eng. 596 (2014) 15–24.
[27] J. Polák, J. Man, Int. J. Fatigue 91 (2016) 294–303.
[28] N. Thompson, N. Wadsworth, N. Louat, Philos. Mag. 1 (1956) 113–126.
[29] R.C. Boettner, A.J. McEvily, Y.C. Liu, Philos. Mag. 10 (1964) 95–106.
[30] A. Heinz, P. Neumann, Acta Metall. Mater. 38 (1990) 1933–1940.
[31] P. Neumann, A. Tönnessen, in: Strength of Metals and Alloys (ICSMA 8), Elsevier, 1989, pp. 743–748.
[32] C. Blochwitz, W. Tirschler, Mater. Sci. Eng. 339 (2003) 318–327.
[33] C. Blochwitz, W. Tirschler, Cryst. Res. Technol. 40 (2005) 32–41.
[34] M.D. Sangid, H.J. Maier, H. Sehitoglu, Int. J. Plast. 27 (2011) 801–821.
[35] M.D. Sangid, Int. J. Fatigue 57 (2013) 58–72.
[36] G. Laplanche, M. Schneider, F. Scholz, J. Frenzel, G. Eggeler, J. Schreuer, Scr. Mater. 177 (2020) 44–48.
[37] T.M. Smith, M.S. Hooshmand, B.D. Esser, F. Otto, D.W. McComb, E.P. George, M. Ghazisaeidi, M.J. Mills, Acta Mater. 110 (2016) 352–363.
[38] M. Heczko, V. Mazánová, R. Gröger, T. Záležák, M.S. Hooshmand, E.P. George, M.J. Mills, A. Dlouhý, Acta Mater. 208 (2021) 116719.
[39] M. Schneider, E.P. George, T.J. Manescau, T. Záležák, J. Hunfeld, A. Dlouhý, G. Eggeler, G. Laplanche, Int. J. Plast. 124 (2020) 155–169.
[40] M. Heczko, J. Polák, T. Kruml, Mater. Sci. Eng. 680 (2017) 168–181.
[41] C. Laird, P. Charsley, H. Mughrabi, Mater. Sci. Eng. 81 (1986) 433–450.
[42] M.S. Pham, C. Solenthaler, K.G.F. Janssens, S.R. Holdsworth, Mater. Sci. Eng. 528 (2011) 3261–3269.
[43] V. Mazánová, M. Heczko, V. Škorík, A. Chlupová, J. Polák, T. Kruml, Mater. Sci. Eng. 767 (2019) 138407.